This project is supported by the European Commission's FP7 Capacities Programme for the period April 2013 - March 2017 under the Grant Agreement number 312495.
www.solarnet-east.eu

DELIVERABLE D70.1

Results of MCAO Correction Simulations

Part I: MCAO Simulations (1/2)

Part II: MCAO Simulations (2/2)

WP 70 Wavefront Control: Turbulence Characterization and Correction

1ST Reporting Period

November 2014

This project is supported by the European Commission's FP7 Capacities Programme for the period April 2013 - March 2017 under the Grant Agreement number 312495.

PROJECT GENERAL INFORMATION

Grant Agreement number: 312495

Project acronym: SOLARNET

Project title: High-Resolution Solar Physics Network

Funded under: FP7-INFRASTRUCTURES: INFRA-2012-1.1.26 - Research Infrastructures for High-Resolution Solar Physics

Funding scheme: Combination of Collaborative Project and Coordination and Support Action for Integrating Activities

From: 2013-04-01 to 2017-03-31

Date of latest version of Annex I against which the assessment will be made: **13/02/2013**

Periodic report: 1st **X** 2nd ☐ 3rd ☐ 4th ☐

Period covered: from **01/04/2013** to **30/09/2014**

Project's coordinator: Dr. Manuel Collados Vera, IAC.

Tel: (34) 922 60 52 00

Fax: (34) 922 60 52 10

E-mail: mcv@iac.es

Project website address: http://solarnet-east.eu/

IAC TECHNOLOGY DIVISION

DO/TN-SNT/019v.1

DOTNSNT_019V1

October 14, 2014

Project Ref.: 312495

PROJECT / DESTINATION:

SOLARNET

TITLE:

WP70.1 MCAO SIMULATIONS 1/2 (D70.1)

INSTITUTO DE ASTROFISICA DE CANARIAS

38200 La Laguna (Tenerife) - ESPAÑA - Phone (922)605200 - Fax (922)605210

AUTHOR LIST

Name	Function
Icíar Montilla	Adaptive Optics Optical Engineer

APPROVAL CONTROL

Control	Name	Function
Revised by:		
Approved by:	Manuel Collados	WP70 Leader
Authorised by:	Manuel Collados Vera	Project Coordinator

DOCUMENT CHANGE RECORD

Issue	Date	Change Description
01	16/09/2014	Initial Issue

SUMMARY

During 2013 and 2014 we have been studying the effects that using correlating wide field sensors has on the AO performance.
Collecting a wide field of view has several implications, i.e. averaging wavefront information from different sky directions, making the Strehl ratio to drop for low elevation observations. So far these effects have not been studied in MCAO, and we dedicated 2013 to that study. We have analysed this effect by using the Fractal Iterative Method (FrIM), which incorporates a wide field Shack-Hartmann, and we have performed simulations of the EST MCAO system to analyse the performance for a large range of elevations, as required in solar observations, and depending on the asterism geometry and number and height of DMs, in order to find the best system configuration. We published that study in RD.1.
During 2014, we modelled the correlating wide field sensor and the way it senses the high altitude turbulence. Thanks to this improved modelling, we made an analysis of the influence of this sensing on the performance of each AO configuration, conventional AO and MCAO. In addition to the analytical study, simulations similar to the case of the EST AO systems with FRiM-3D (the Fractal Iterative Method for Atmospheric Tomography) were used in order to highlight the relative influence of design parameters. In particular, the results showed the performance evolution when increasing the telescope diameter. We analysed the effect of high altitude turbulence correlation showing that increasing the diameter of the telescope does not degrade the performance when correcting on the same spatial and temporal scales. This study was presented in RD.2.

TABLE OF CONTENTS

LIST OF ABBREVIATIONS

AO	Adaptive Optics
MCAO	Multi Conjugate Adaptive Optics
EST	European Solar Telescope
WFS	Wave Front Sensor
HOWFS	High Order Wave Front Sensor
LOWFS	Low Order Wave Front Sensor
DM	Deformable Mirror
FOV	Field Of View
SCAO	
SHWFS	Shack Hartmann Wave Front Sensor
WFWFS	Wide Field Wave Front Sensor

1. INTRODUCTION: THE MCAO SYSTEM OF THE EST

The European Solar Telescope (EST) will be built to perform accurate high-spatial and high-temporal resolution polarimetry in many wavelengths simultaneously to study the magnetic coupling of the solar atmosphere, from the photosphere up to the upper chromosphere. It will reach the required spatial accuracy thanks to its built-in MCAO module, that will provide a corrected 1 arcmin field-of-view with 50% Strehl at 500 nm. To reach such a Strehl we need to deal with some of the challenges of solar AO, as compared to night-time AO. Due to the fast evolving daytime seeing conditions and the fact that most science is done at visible wavelengths, a very high closed-loop bandwidth is required to achieve solar AO correction. The high temporal frequency content of the wavefront fluctuations leads to required sampling rates of 2 kHz or more. This, along with the fact that solar AO systems need a large number of corrective elements in spite of the relatively small, compared to night-time telescopes, apertures of solar telescopes, gives systems that approach the complexity of what is referred to as extreme AO [RD.3]. The optical layout of the EST features two main adaptive optics modes: the conventional AO (CAO) and the Multi-Conjugate AO mode (MCAO) [RD.4]. The CAO mode uses the ground layer DM and a high order correlating Shack-Hartmann wavefront sensor (HOWFS). The MCAO mode uses five DMs at conjugate heights of 0 km (ground layer DM) and 1.6, 6.6, 10 and 23 km. It uses the high order sensor for the centre of the FOV and one wide field low order sensor (LOWFS), with less sub-apertures but wide FOV, that senses the field dependent and weaker aberrations of the high altitude turbulence. The pupil and focus geometry of both Wavefront Sensors, with a reduced number of subapertures, is shown in Figure 1. The main parameters of the system are displayed in Table 1. A similar approach was proposed for the German Vacuum Tower Telescope [RD.5] and GREGOR MCAO systems [RD.6].

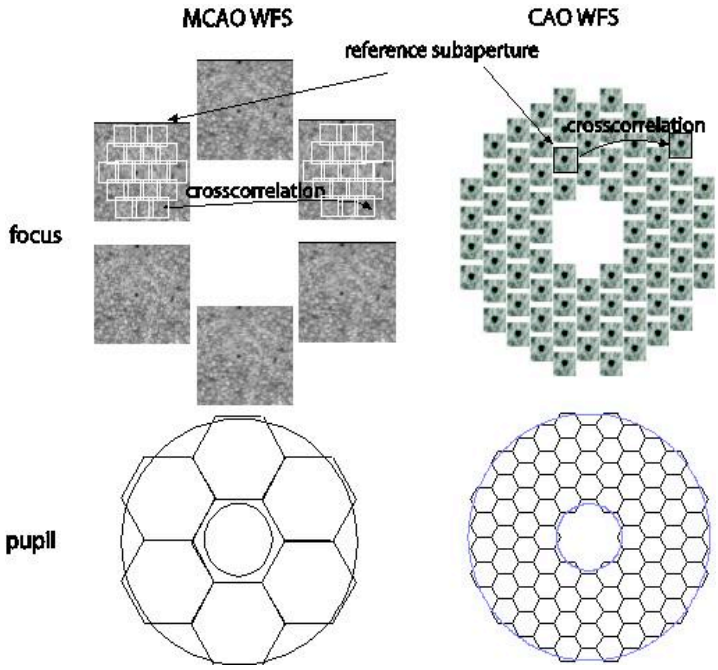

Figure 1: High-order narrow-field SH WFS and low-order wide-field SH WFS concept

Parameter	AO	MCAO
DM heights (km)	0	0, 1.6, 6.6, 10, 23
Spatial sampling (cm)	8	8, 30, 30, 30, 30
Sensing field points	1	19
FOV (arcsec)	8	60
Subaps/metapupil diameter	50	50, 15, 20, 23, 36

Table 1: EST AO configuration parameters

Correlating sensors collect a wide field of view, which has several implications, i.e. averaging wavefront information from different sky directions, making the Strehl ratio to drop for low elevation observations. We have studied these effects performing end-to-end simulations of the EST MCAO system to analyse the performance for a large range of elevations, as required in solar observations, and depending on the asterism geometry and number and height of DM's, in order to find the best system configuration.

2. THE PROBLEM OF THE INTRINSIC ANISOPLANATISM ASSOCIATED TO THE SOLAR WAVEFRONT SENSOR

One of the challenges of solar AO is that the wavefront sensor has to work on extended and low contrast objects such as sunspots or solar granulation. A correlating Shack-Hartmann is used to sense the wavefront. The FOV has to be large enough to contain structure for the correlation algorithm to work robustly, but not too large, to avoid averaging of wavefront information from the upper layers of the atmosphere. Usually a FOV of 8-10 arcsec is used. With such FOV, the anisoplanatism affects the measurements of the correlating SHWFS, averaging the wavefront information over the field of view and thus decreasing the sensitivity to wavefront distortions introduced at large heights above the telescope aperture. For low elevation observations, the increased line-of-sight distance to the turbulent layers leads to a wider wavefront area to be averaged for a given FOV. Therefore, the contribution of this anisoplanatism to the AO measurements must be taken into account in solar AO performance evaluation. This was never done before the starting of AO studies for the 4-m class solar telescopes. So far no analytical formulas include the wavefront sensor anisoplanatism error in the error budget and in the error model used to perform the simulation. Therefore, the only way to estimate its effect is numerically, by including an end-to-end model of the wide field cross-correlation WFS in the simulations.

2.1 PERFORMANCE ANALYSIS

We performed open-loop simulations for different telescope elevations with the Fractal Iterative Method (FrIM3D), a fast algorithm for tomographic wavefront reconstruction developed at CRAL. In this case we have reconstructed layers at the altitude of the DMs (no projector was used). The simulations featured 10 realizations of a turbulent atmosphere with r_0=10 cm at 550 nm. The atmosphere includes 19 frozen layers distributed in altitude, representative of typical atmospheric conditions during solar observations. This r_0 is maintained for all the elevations, and the reason is that solar telescopes observe at low elevation during the first hours of the day, and at that moment the atmosphere is less turbulent. Therefore, we use the same value for 15º elevation than for the zenith. The atmospheric profile is the combined C^2_n profile from Rimmele (RD.3). Both the narrow field HOWFS and the wide field LOWFS are simulated. The correlating SHWFS was simulated providing an approximate average of the measurement over a 10 arcsec field of view, in order to include the anisoplanatism effect. Only the fitting error, that is the error term due to the limited number of actuators, is considered in these simulations. The results are plotted in Figure 2. These simulations show the homogeneous correction over the 1 arcmin FOV that FrIM3D is able to give. The reduction in the Strehl for low elevations is an effect of the intrinsic anisoplanatism associated to wide field WFSs and the generalized fitting error.

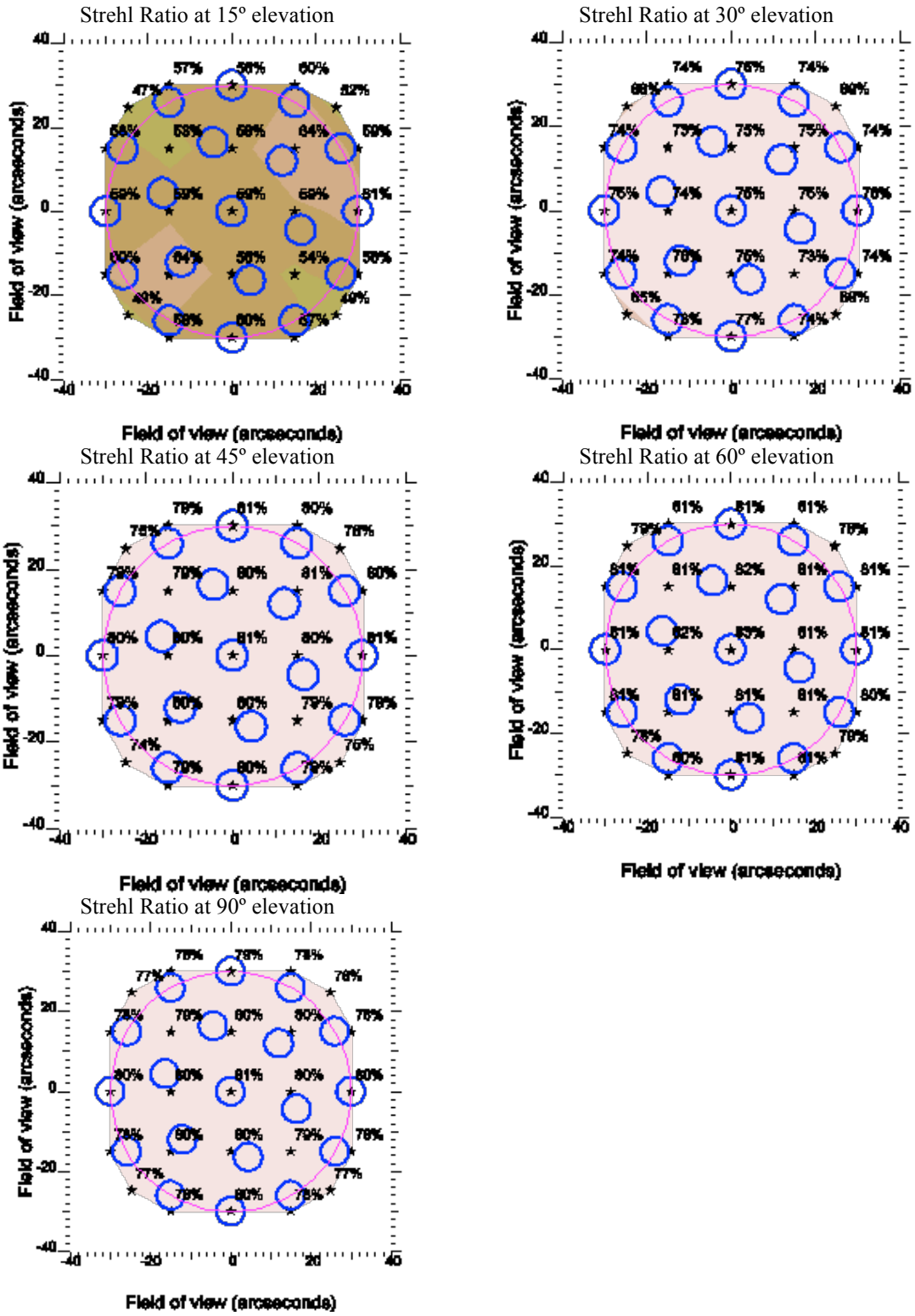

Figure 2: Strehl ratio for different elevation angles. The blue circles are the centres of the WFWFS subfields. The pink circle is the 1 arcmin FOV. The stars are used to probe the Strehl

2.2 ESTIMATED PERFORMANCE INCLUDING THE ERROR BUDGET

We have estimated the Strehl ratio including the fitting, temporal delay, WFS measuring and bandwidth errors, using the values shown in Table 2.
The temporal delay error, in case no temporal prediction is made, can be estimated using the following expression:

$$\sigma^2_{delay} = 0.962\left(\tau/\tau_0\right)^{5/3}$$

where τ is the delay and τ_0 the coherence time of the atmospheric turbulence.
The WFS measuring error can be estimated with the following equation:

$$\sigma^2_{WFS} = \frac{5m^2}{4n_r^2 \cdot contrast^2 \cdot SNR^2}$$

where m is the width of the reference subimage autocorrelation function in pixels, n_r is the subimage size in pixels, SNR is the signal-to-noise ratio, and the contrast is the is the measured contrast of the observed solar scene.

λ (nm)	**τ_0 (ms)**	**Frequency (kHz)**	**SNR**	**contrast**	**f_S (kHz)**	**f_G (Hz)**
550	2	2	223	3%	1	213

Table 2: MCAO simulation parameters

The bandwidth error is due to the limited correcting bandwidth of the AO system. The bandwidth error is proportional to the ratio between the frequency of the turbulence, quantified by the Greenwood frequency f_G , and the bandwidth f_S of the AO system:

$$\sigma^2_{BW} = \left(\frac{f_G}{f_S}\right)^{5/3}$$

In the special case of a single turbulent layer moving at a speed v, the Greenwood frequency f_G can be written:

$$f_g = 0.427\,\frac{v}{r_0}$$

In general, closed loop bandwidths in excess of 100 Hz are required for solar AO systems.
In Figure 3 we have plotted the Strehl in function of the field for different elevations. At the left we show the results of a CAO simulation for the EST and at the right the MCAO results. We see that **in spite of the effect of the anisoplanatism of the 10 arcsec correlating SH still a homogeneous correction is obtained at 15^o elevation with a Strehl of 40% using an MCAO system**.

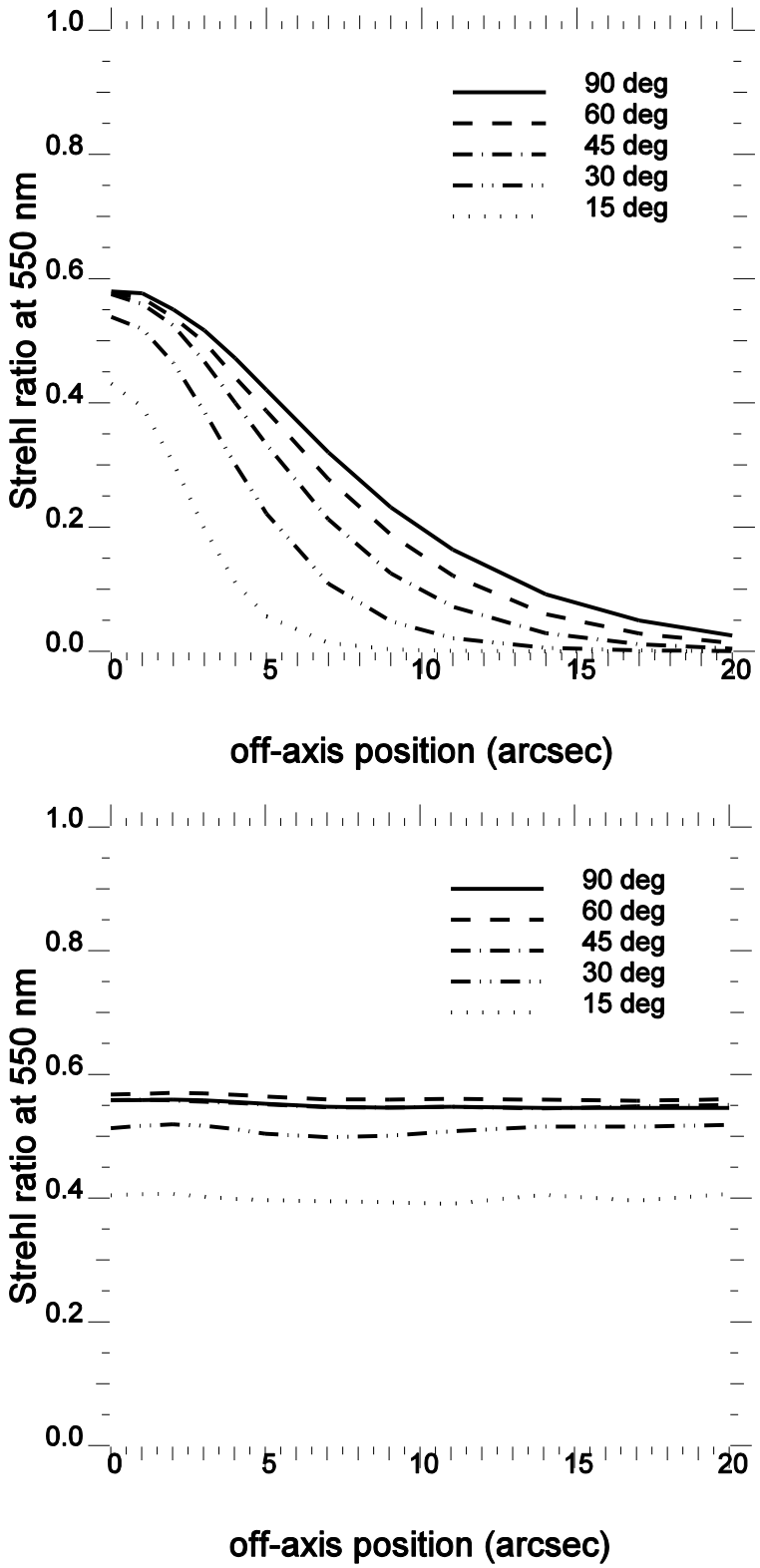

Figure 3: Estimated performance including the fitting, temporal delay, WFS measuring and bandwidth errors

3. MODELLING THE EFFECT OF THE HIGH-ALTITUDE TURBULENCE

One of the challenges of solar AO is that the wavefront sensor has to work on extended and low-contrast objects such as sunspots or solar granulation. A correlating Shack-Hartmann is used to sense the wavefront. The FOV has to be large enough to contain structure for the correlation algorithm to work robustly, but not too large, to avoid averaging of wavefront information from the upper layers of the atmosphere. Usually a FOV of 8-10 arcsec is used. With such FOV, the anisoplanatism affects the measurements of the correlating Shack-Hartmann Wave Front Sensor (SHWFS), averaging the wavefront information over the field of view and thus decreasing the sensitivity to wavefront distortions introduced at large heights above the telescope aperture. For low elevation observations, the increased line-of-sight distance to the turbulent layers leads to a wider wavefront area to be averaged for a given FOV. Therefore, the contribution of this anisoplanatism to the AO measurements must be taken into account in solar AO performance evaluation, as was done in Bechet et al. (RD.7) and Montilla et al. (RD.1).

In this section we analyse more in depth the problem of the high-altitude turbulence sensing. We model the correlating wide field sensor and the way it senses the high altitude turbulence in order to understand how the performance changes with the diameter of the aperture.

3.1 PERFORMANCE SIMULATIONS WITH 1 LAYER AND SCAO CORRECTION

To understand the effect of sensing the high altitude turbulence with a WFWFS we have first simulated an atmosphere with 1 high altitude layer and 1 DM at the pupil (see Table 3). Our atmosphere follows the von Karman statistics, therefore it has a non-infinite outer scale. We have set a value of L_0=25 m. The outer scale determines the magnitude of the overall tilt component of atmospheric turbulence (RD.8). When is not the case that L_0 >> D the tilt will be smaller than predicted by Kolmogorov (RD.9) as can be seen in Figure 4.

layer height (km)	8
DM height (km)	0
r_0 (cm)	50
C_n^2	1
L_0 (m)	25
subaps (cm)	4
elevation (deg)	30
WFWFS FoV (arcsec)	10

Table 3: 1 layer atmosphere parameters

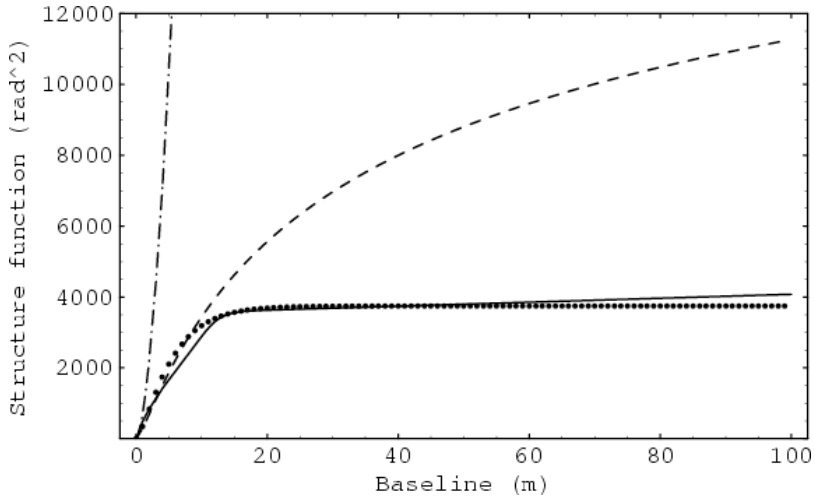

Figure 4: Phase structure function from A. Ziad et al. (RD.9). We can see the difference among the Kolmogorov model (dashed dotted line) and the von Karman model (dotted line) for L_0=25 m

The results of the simulations are shown in Figure 5, where we have plotted the variance of the error due to the sensing of the high altitude turbulent layer with a WFWFS, σ^2_{wfwfs}. We clearly see that the error grows for diameters smaller than the projection of the FOV, and how for larger diameters it converges towards the fitting error given by the size of the projection of the FOV at the height of the high-altitude turbulence layer. Assuming that the projection of the field is larger than the subapertures, there will be many actuators for each subpupil. Then we can say that the influence function will be similar to a Gaussian, and the variance of the fitting error will follow the equation:

$$\sigma^2_{fitting} = 0.23\left(d/r_0\right)^{5/3}$$

where d is the diameter of the projection of the WFWFS FOV on the high-altitude layer,

$$d = h \cdot \tan\theta_{fov} \cdot \sin\phi$$

being h the height of the layer, θ_{fov} is the WFWFS FoV and ϕ is the elevation of the telescope.
The variance of the von Karman fitting error follows the equation:

$$\sigma^2_{fitting} = \frac{0.23}{cte_{vonK}\left(\theta_{fov}, h, L_0, r_0\right)}\left(\frac{h \cdot \tan\theta_{fov} \cdot \sin\phi}{r_0}\right)^{5/3}$$

where cte_{vonK} (θ_{fov}, h, L_0, r_0) is the correction factor that we need to apply to find the value of the fitting error constant for von Karman statistics, that for an outer scale of 25 m, a projection diameter of 80 cm and r_0 of 50 cm has a value of approximately 2. With that value, the variance of the fitting error is 0.24 rad^2.

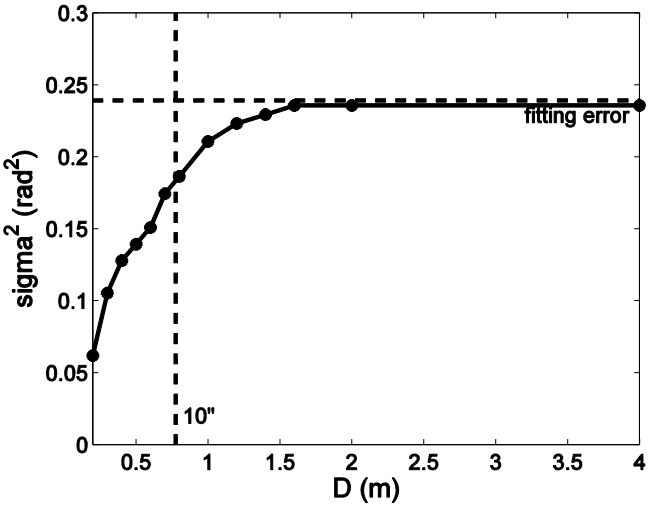

Figure 5: error variance for a 30 deg elevation angle and a 10 arcsec FoV of the WFWFS

From the numerical fitting error variance curve of Figure 5 we can obtain the curves for different WFWFS FOVs and layers at different heights and with different values of r_0, following the law:

$$\sigma^2_{wfwfs}\left(D,\theta'_{fov},h',r'_0\right)$$
$$=\sigma^2_{wfwfs}\left(D\frac{d'\left(\theta'_{fov},h',\phi'\right)}{d\left(\theta_{fov},h,\phi\right)},\theta'_{fov},h',r'_0\right)\frac{cte_{vonK}\left(\theta_{fov},h,L_0,r_0\right)}{cte_{vonK}\left(\theta'_{fov},h',L_0,r'_0\right)}\left(\frac{d'\left(\theta'_{fov},h',\phi'\right)}{d\left(\theta_{fov},h,\phi\right)}\right)^{5/3}\left(\frac{r_0}{r'_0}\right)^{5/3}$$

In Figure 6 we show the error variance for a 30º elevation angle, r_0 50 cm at zenith, and 10 arcsec FoV of the WFWFS, calculated with the previous equation and obtained from simulations, for comparison.

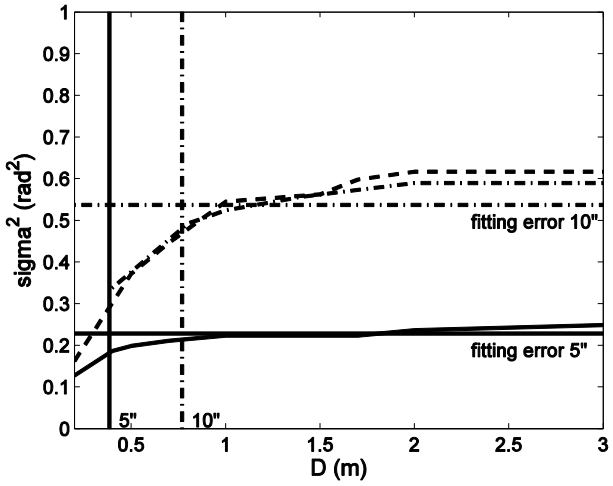

Figure 6: Error variances for a 30º elevation angle, r_0 50 cm at zenith and 5 and 10 arcsec FOV of the WFWFS. The dash-dotted line is calculated from the 5 arcsec curve, using the equation. The dashed line is obtained from simulations.

3.2 PERFORMANCE SIMULATIONS WITH A DAYTIME PROFILE AND MCAO CORRECTION: APPLICATION TO THE EST

The expression of the generalized fitting error variance for an atmosphere with several layers is:

$$\sigma^2_{wfwfs}(D,\theta_{fov}) = \int \sigma^2_{wfwfs}\left(D,\theta_{fov},h,r_0(h)\right)dh$$

Using this equation to compute the generalized fitting error variance for the EST case with the parameters given at Table 1, for an elevation of 30º, we find:

$$\sigma^2_{wfwfs}(4{,}30) = 0.07\ rad^2$$

Adding the fitting error of the ground layer, that is equal to 0.20 rad^2, we have a total error variance of 0.27 rad^2. The variance of the error resulting from the simulations presented at Section 2.1 was 0.29 rad^2. Therefore, with the analytical expression we obtain a Strehl that is only 1% larger than that obtained numerically.

3.3 UNDERSTANDING THE SENSING OF THE HIGH-ALTITUDE TURBULENCE

In this Section we will try to explain the effects on the performance that we have seen in the previous sections. We observe two limiting cases (see Figure 7): when the telescope diameter is smaller than the projection of the FOV on the upper layer, and when it is much larger than it. In the first case, the tip-tilt information is acquired from a surface bigger than the telescope diameter, but it is corrected on the telescope aperture, giving rise to an error, for small diameters, larger than the error when only the tip-tilt is corrected.

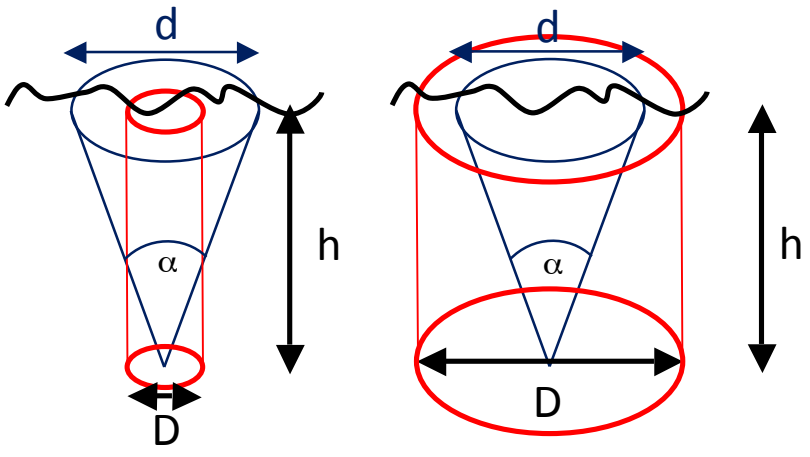

Figure 7: limiting cases for the sensing of the high altitude turbulence: left, telescope diameter much smaller than the projection of the FOV; right, , telescope diameter much larger than the projection of the FOV

As the diameter of the aperture approaches the projection of the FOV on the layer, the error approaches that of a system where only the tip-tilt is corrected, and at a certain point it starts to be smaller, because the system starts to be able to correct more modes. When the diameter of the telescope is much larger than the projection of the FOV on the upper layer, the extended field has an effect on the fitting error, that will be limited by the size of the projection, as can be seen in Figure 8.

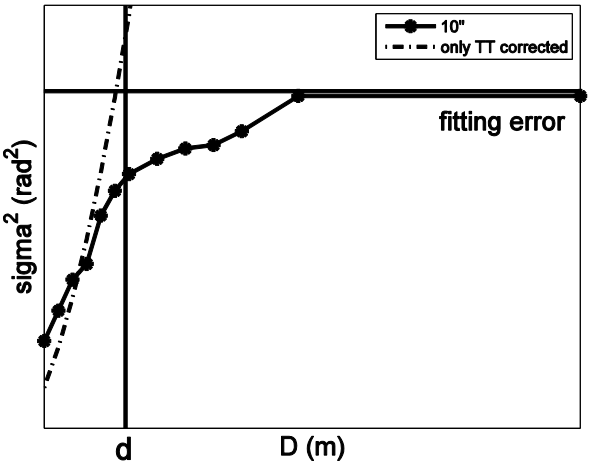

Figure 8: error variance for Kolmogorov statistics

4. CONCLUSIONS

In Section 2 we have shown open-loop preliminary reconstruction results to study the impact of the intrinsic anisoplanatism of the correlating SHWFS on the performance of MCAO systems. The decrease in the Strehl going to lower elevations is observed to be very similar to the SCAO case, meaning that the anisoplanatism error dominates the performance. But in closed-loop MCAO, the anisoplanatism effect on measurement is expected to decrease and it is required to pursue this study in order to understand if MCAO closed-loop correction could mitigate the anisoplanatism effect. Nevertheless, an homogeneous 40% Strehl over the 1 arcmin FoV was obtained with FrIM3D.

In 3 we have analysed the effect of high altitude turbulence correlation on the performance of a solar AO system, and we have proved that increasing the diameter of the telescope does not degrade the performance when correcting on the same spatial and temporal scales. When the diameter of the telescope is much smaller than the projection of the FOV of the WFWFS on the upper layers, we cannot even fully correct the tip-tilt in the aperture, and the order of the error is larger than that corresponding to tip-tilt correction. For telescope diameters larger than the projection of the FOV of the WFWFS on the upper layers, what limits the performance of the system is the diameter of the projection of the FOV of the WFWFS on the layers, not the size of the subapertures. The reduction in the Strehl for low elevations is an effect of the generalized fitting error. Therefore, we need to consider this parameter, and not only the r_0, when designing a MCAO system for a solar telescope, and when predicting its performance. In the future we plan to calculate the analytical expression of the variance of this fitting error in order to use that information to do a better design of future large solar telescopes AO systems.

ANNEXES

A. LIST OF REFERENCE DOCUMENTS

RD.1	Montilla, I.; Béchet, C.; Langlois, M.; Tallon, M.; Collados, M., "Preliminary performance analysis of the Multi-Conjugate AO system of the EST", AO4ELT3, Florence, Italy, 2013
RD.2	Montilla, I.; Tallon, M.; Langlois, M.; Béchet, C.; Collados, M., "Modelling the effect of high altitude turbulence in wide-field correlating wavefront sensing and its impact on the performance of solar AO systems", SPIE 9148, Montreal, Canada, 2014
RD.3	Rimmele, T.; Marino, J.; Living Reviews in Solar Physics 8, (2011), 2
RD.4	Collados, M.; Bettonvil, F.; Cavaller, L.; Ermolli, I.; Gelly, B.; Pérez, A.; Socas-Navarro, H.; Soltau, D.; Volkmer, R., Astronomische Nachrichten
RD.5	O. von der Lühe, T. Berkefeld, D. Soltau, Comptes Rendus Physique 6, (2005) 1139
RD.6	T. Berkefeld, D. Soltau, O. von der Lühe, Multiconjugate solar adaptive optics with the VTT and GREGOR, SPIE Conference 6272 (2006)
RD.7	Béchet, C., Tallon, M., Montilla, I., and Langlois, M., "Wide-field wavefront ensing in solar adaptive optics : modeling and effects on reconstruction", Adaptive Optics for ELTs III (2013)
RD.8	Hardy, J. W., [Adaptive Optics for Astronomical Telescopes], Oxford University Press (1998)
RD.9	Ziad, A., Borgnino, J., Martin, F., Maire, J., and Mourard, D., "Towards the monitoring of atmospheric turbulence model", Astronomy and Astrophysics 414, (2004)

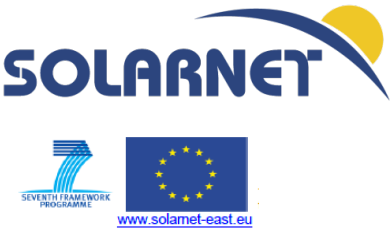

IAC TECHNOLOGY DIVISION

DO/TN-SNT/020v.1

DOTNSNT_020V1

October 14, 2014

Project Ref.: 312495

PROJECT / DESTINATION:

SOLARNET

TITLE:

WP70.1 MCAO SIMULATIONS 2/2 (D70.1)

INSTITUTO DE ASTROFISICA DE CANARIAS

38200 La Laguna (Tenerife) - ESPAÑA - Phone (922)605200 - Fax (922)605210

AUTHOR LIST

Name	Function
Luzma Montoya Martínez	Optical Engineer

APPROVAL CONTROL

Control	Name	Function
Revised by:		
Approved by:	Manuel Collados Vera	WP70 Leader
Authorised by:	Manuel Collados Vera	Project Coordinador

DOCUMENT CHANGE RECORD

Issue	Date	Change Description
01	22/09/2014	Initial Issue

SUMMARY

Although multi-conjugate adaptive optics (MCAO) has been proven for night astronomy at infrared wavelengths, there are important differences with respect to solar astronomy that must be considered. Non-linear effects due to phase propagation in infrared wavelengths are negligible while become important for visible wavelengths. MCAO systems for night astronomy conjugate the deformable mirrors (DM) in the same order of turbulence layer occurrence. However, it has been claimed in the literature (Flicker, RD.2), that at optical wavelengths and at low elevation angles, this correction must be done in the inverse order of turbulence layers occurrence to avoid the non-linear effect of phase propagation.

With the aim of verifying the influence of the DMs sequence in a MCAO system, we have analyzed two different approaches using the ZEMAX tool. We also developed a script in *yorick* which includes the effects of amplitude and phase propagation.

One of the priority goals to attain within the frame of SOLARNET work package WP70.1 is to build a simulation environment suitable for Solar MCAO. We benefit from the expertise on MCAO for night astronomy. We are currently adapting two existing MCAO codes, YAO and FRiM for the Solar case.

TABLE OF CONTENTS

LIST OF ABBREVIATIONS

AO	Adaptive Optics
DM	Deformable Mirror
MCAO	Multi-conjugate Adaptive Optics
OPD	Optical Path Difference
OPL	Optical Path Length
WFS	Wavefront sensor
WP	Work Package

1. WAVE PROPAGATION IN SOLAR ASTONOMY

A wave propagated in a turbulent media suffers from amplitude and phase perturbations. Two regimes can be defined depending on propagation distance. If propagation distance (z) is long (far-field approximation) i.e. $z >> D^2/\lambda$, with D the telescope diameter and λ the wavelength, wave changes equally in phase and amplitude as described by Fraunhofer diffraction. If the propagation distance is short (near-field approximation) i.e. $z << D^2/\lambda$, amplitude perturbations are small compared with phase perturbation because of Fresnel diffraction.

It has been shown that near-field approximation is valid for most astronomical applications, and therefore scintillation effects are negligible (Young, RD.1). But strong phase perturbations introduce amplitude variations due to diffraction, that can be corrected with phase modulators as addressed by Fouche et al. (RD.3).

In a MCAO system each DM is conjugated with a turbulent layer. There are two options to place the DMs in the optical train of the MCAO system, as it is shown in Figure 1: (a) correcting the layers in the inverse order to conjugation ("inverse correction") and (b) correcting the layers in the same order as they are optically conjugated (we refer to this option as "direct correction").

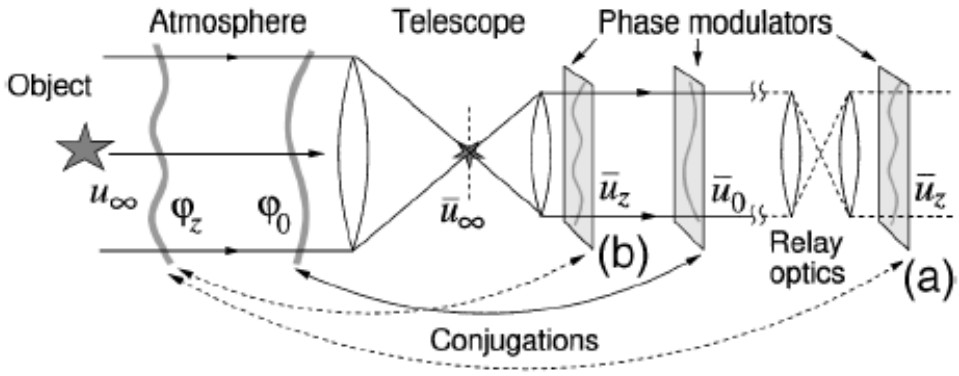

Figure 1.Schematic two-DM MCAO setup. (a) inverse correction (b) direct correction. (Flicker,RD.2)

A total cancellation of phase and amplitude is only achieved when applying inverse correction. MCAO system for infrared night astronomy obtains high performances using the direct correction. But it has been claimed in the literature (RD.2) that direct correction degrades for visible wavelengths and low elevation angles (Figure 2), and that this degradation is due to amplitude fluctuations originated by the wavefront propagation as pointed before.

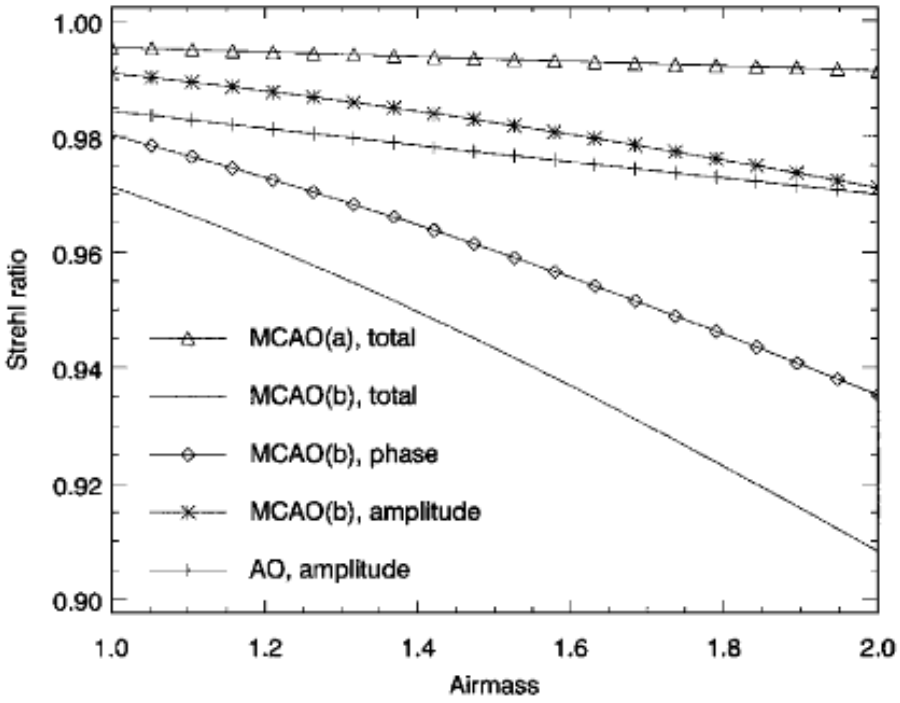

Figure 2. Strehl ratio as a function of airmass for 500nm wavelength. (Flicker RD.2)

The purpose of this study is to analyze the performance of the sequence of DMs correction in a MCAO system at visible wavelengths. For this analysis the results obtained with ZEMAX tool are compared with the script developed in *yorick* at IAC.

1.1 Analysis of wave propagation with ZEMAX tool

Most of the AO simulators are based on Monte Carlo methods and physical optics model. The powerful optical design tool ZEMAX is firstly employed to test the performance of a simple MCAO as a function of DM sequence correction. To this end, two optical setups are designed. The first setup is based on paraxial optics and the second one is based on wavefront propagation through surfaces in the entrance space.

The objective is to study the non-linear effects due to phase propagation, therefore is out of the scope to simulate the wavefront sensor (WFS) and real DMs. The wavefront is propagated trough discrete phase screens. Each phase screen introduces a phase difference, correction is simulated with the same phase screens but with opposite sign.

Phase screens have been simulated with IDL code based on Kolmogorov model by Fast Fourier Transform (FFT) methods (see Figure 3).

Phase screens are introduced in ZEMAX as "Grid Phase". The phase screen generated in IDL has to be transformed into a ".int" file. This file contains a vector with the phase values specified from $-x$ to $+x$ starting at $+y$ edge of the grid. Thereafter, the ".int" file is converted into a ".dat" file in ZEMAX.

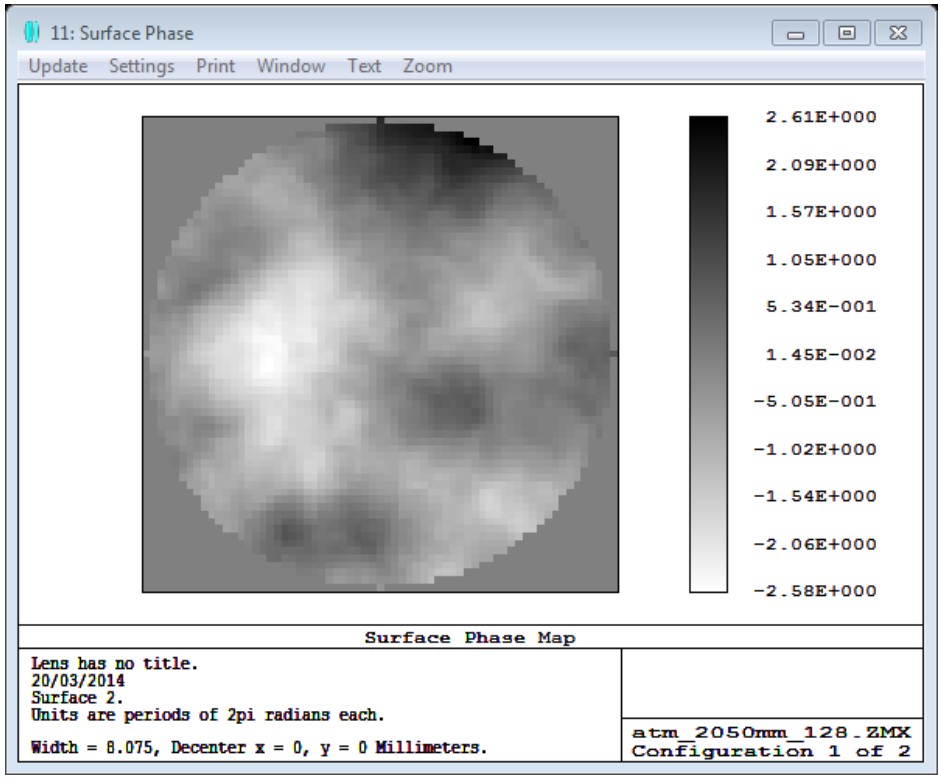

Figure 3. Phase screen simulated with IDL and transformed into ZEMAX

1.1.1 Paraxial approach

The setup is based on paraxial elements and a point-like source. A two turbulent layers model is simulated as shown in Figure 1.The system is designed so that the pupil size keeps constant to avoid rescaling the phase screens.

In the direct case two paraxial lenses are used with focal length equal to 100 mm (F/4) and pupil diameter of 50 mm. Two phase screens are separated by 90 mm. The phase errors are of the order of few wavelength, which is a pessimistic case.

In the inverse case, Layer 2 is corrected after the first paraxial system (similar to the direct case), the Layer 1 is corrected after a reimaging system composed of two paraxial surfaces.

The Figure 4 represents the irradiance of the propagated wavefront through the surfaces in the direct case. The simulation is performed with a 25mm top hat beam and total power of 1W. It can be seen how the amplitude varies after propagation.

Irradiance after Layer 1

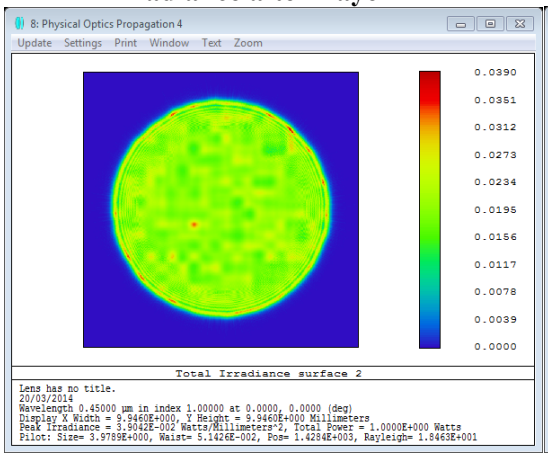

Irradiance after Layer 2

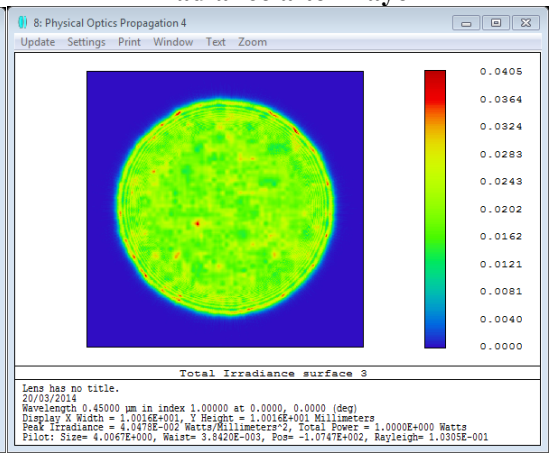

Irradiance after paraxial system

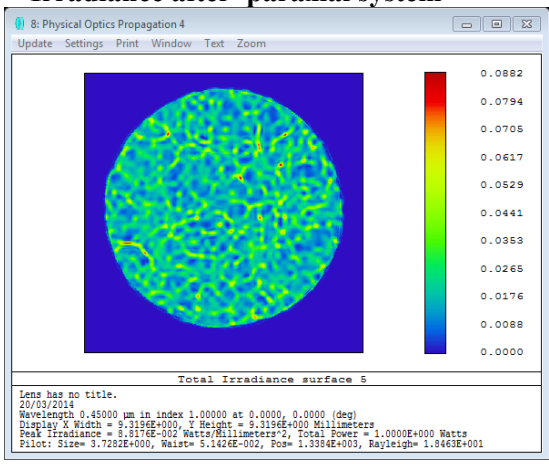

Irradiance after correction of Layer 1

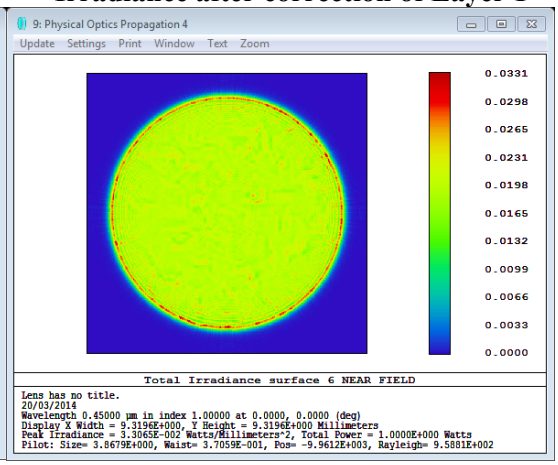

Figure 4. Irradiance of propagated beam trough the optical surfaces in the direct case correction.

Figure 5 shows the residual phase and irradiance for the direct and inverse cases. In the direct correction case, there are residuals in amplitude and phase, opposite to what is seen for the inverse case. In the direct case, the phase of any point of the higher layer does not cancel with the corresponding point in the conjugated image due to the distortion introduced by the lower turbulent layer.

Residual Irradiance after direct correction **Residual Phase after direct correction**

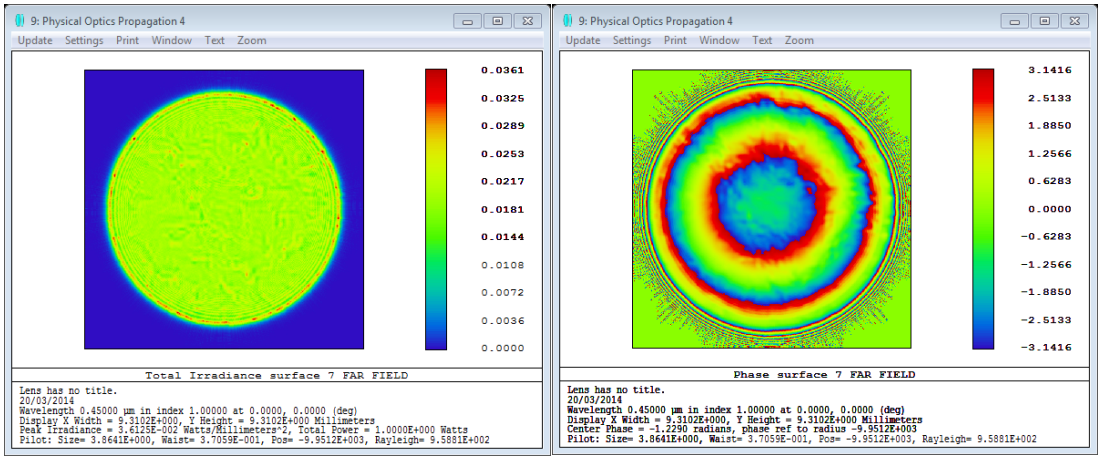

Residual Irradiance after inverse correction **Residual Phase after inverse correction**

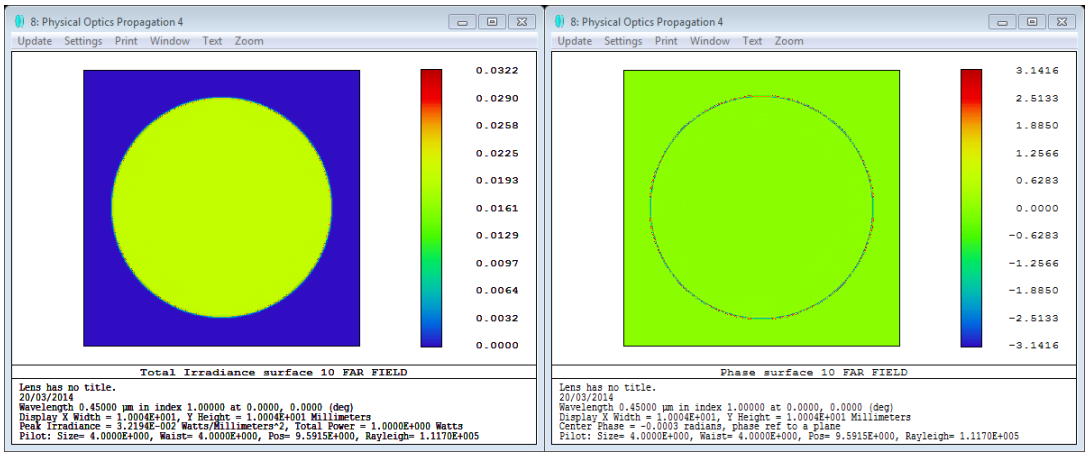

Figure 5.Residual Irradiance and phase resulting from direct correction (top) and inverse correction (bottom).

The encircled energy and spot diagram are analysed in the image plane. As seen in Figure 6, the diffraction limit is achieved in the direct case but not in the inverse case. However, analyzing the diffraction encircled energy indicates that both cases degrade with respect to diffraction limit (Figure 7). The residual wavefront map at the image plane in the inverse case should be zero but, as seen in Figure 8, this is not the case. This is due to the way that

ZEMAX calculates the optical path difference (OPD) and hence wavefront errors for paraxial systems.

In conclusion, the paraxial approach simulated in ZEMAX is not appropriated to estimate the MCAO correction of two turbulent layers in the direct case (WF firstly corrected by the DM conjugated with the higher layer and then by the DM conjugated with a lower layer) or in the inverse case.

Direct case

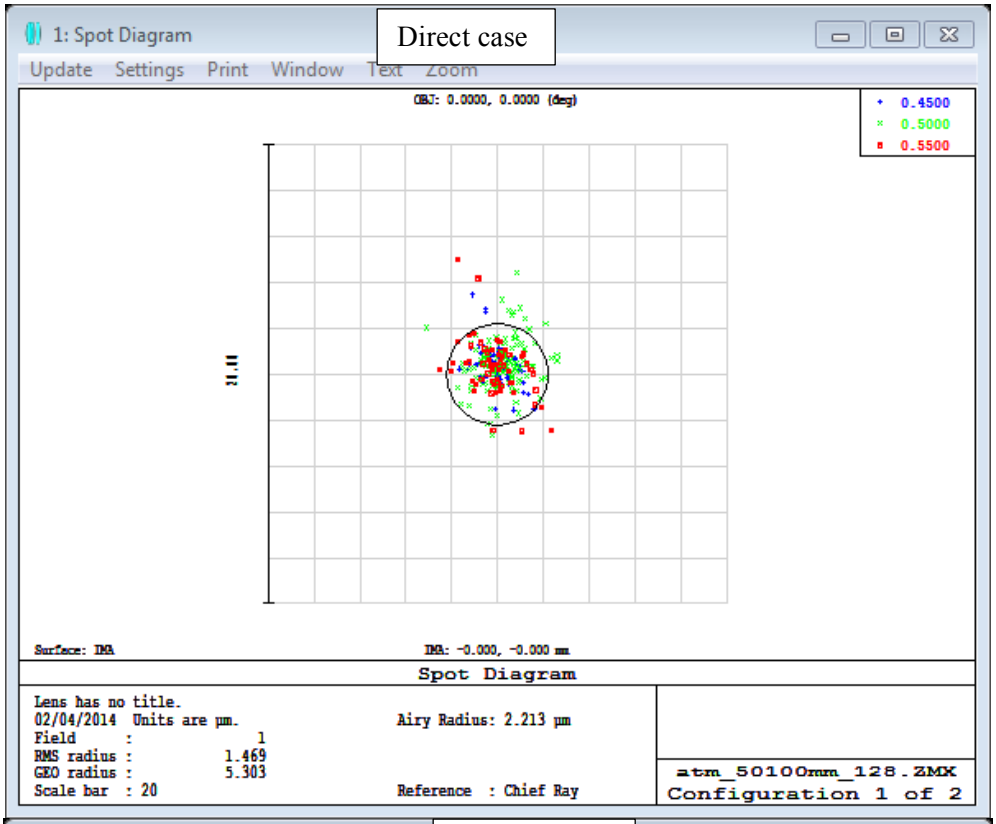

Inverse case

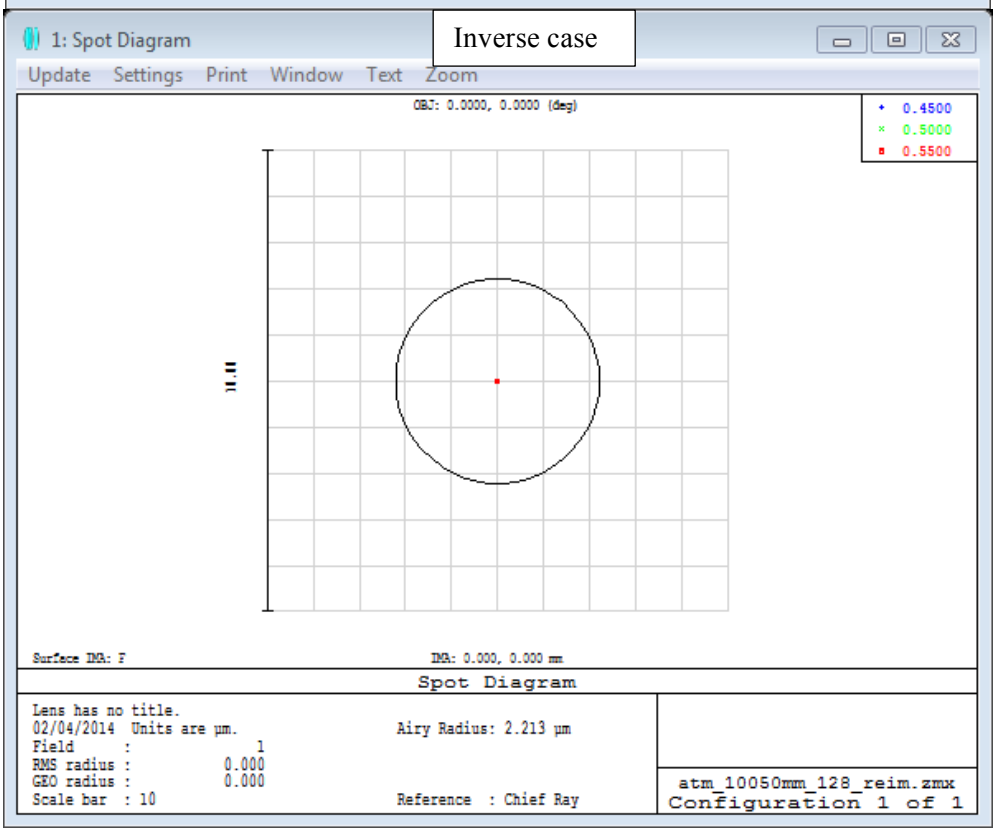

Figure 6.Spot diagram in image plane for direct case(top) and inverse case (bottom).

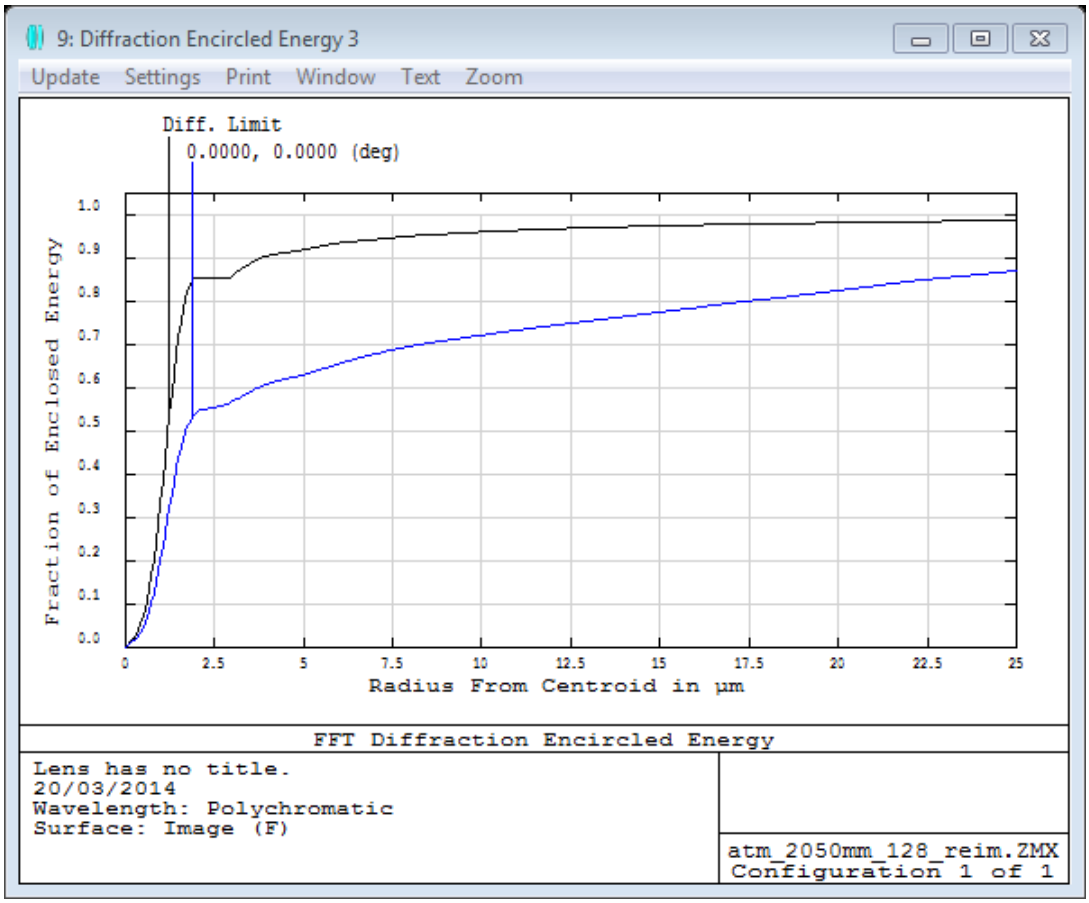

Figure 7. Diffraction Encircled Energy. Blue line: direct and inverse case, black line: diffraction limited case

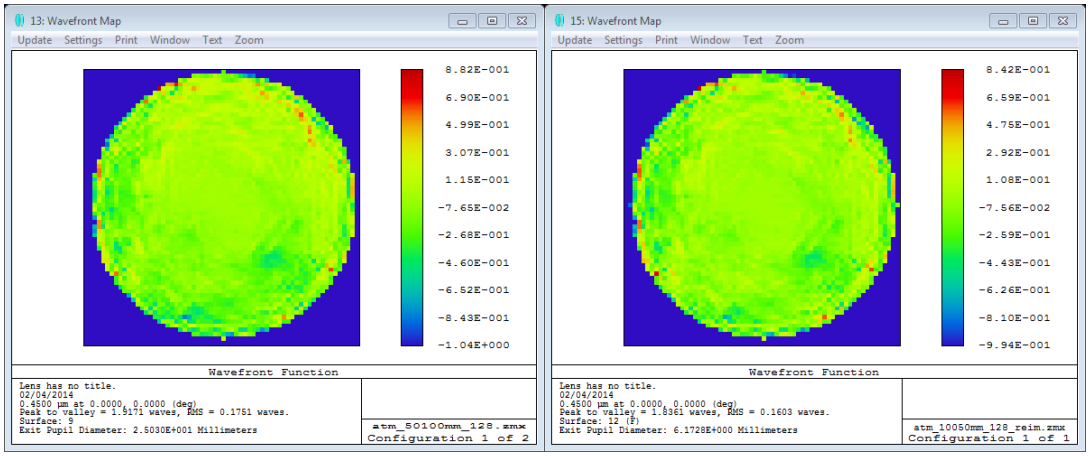

Figure 8. Residual wavefront map in image plane for direct case (left) and inverse case (right)

1.1.2 Entrance Space approach

Another approach to address the problem with ZEMAX consists on simulating an afocal propagation system in the entrance space as shown in Figure 9. One turbulent layer is simulated at 1km and another one at 15km. The correction is performed by using the same phase screens but with opposite signs. Blue lines represent the inverse correction (screen1-screen2-pupil-screen2-screen1). Red lines represent the direct correction (screen1-screen2-pupil-screen1-screen2).

In the case of direct correction the complex field arriving from screen1 is disturbed by screen2 so that the correction to be applied in the plane of screen 1 does not cancel the non linear effects. In the inverse correction case the optical path difference is zero, contrary to the direct correction case. The propagation of layer 2 is not disturbed since there is no turbulence between the layer and the pupil. Then the phase contribution of that layer is corrected in the plane of screen2, only the turbulent phase due to the contribution of screen1 remains. In the inverse case each layer contribution is isolated and corrected separately .

For this simulation phase screens of 5m wide on a grids of 128x128 elements, with average r0 of 10 cm are used. The entrance pupil is of 4 meter diameter.

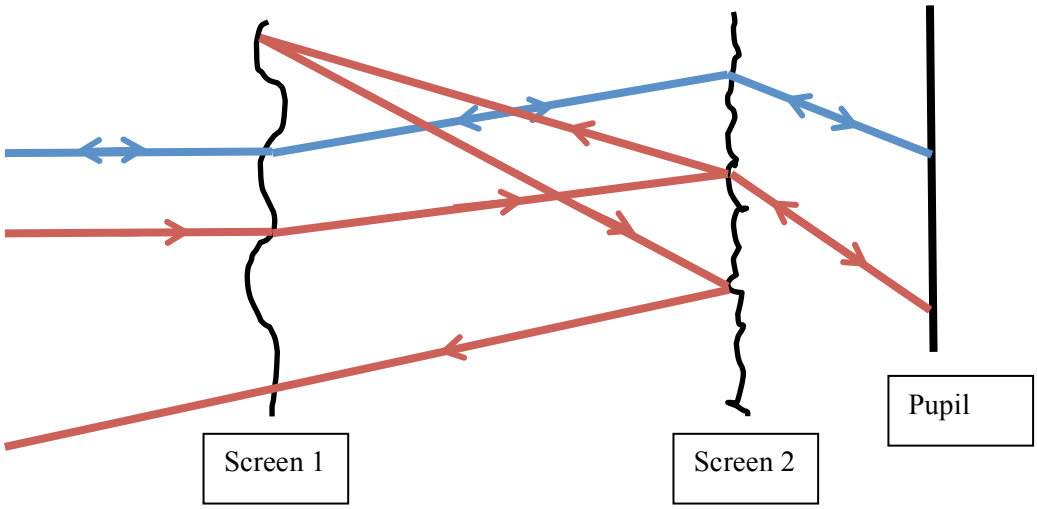

Figure 9. Scheme of geometric ray propagation in the entrance space. Blue: inverse case, Red: direct case.

Figure 10 represents the spot diagram and residual wavefront map in the image plane for the direct and inverse cases. The correction in the inverse case is perfect and the residual wavefront error is zero, while in the direct case the correction, although very good (e.g. rms

error = 0.0081 waves) is not perfect as seen in the Strehl ratio values showed in Table 1. Amplitude fluctuations have been [illegible] inverse case (Figure 11).

No correction case

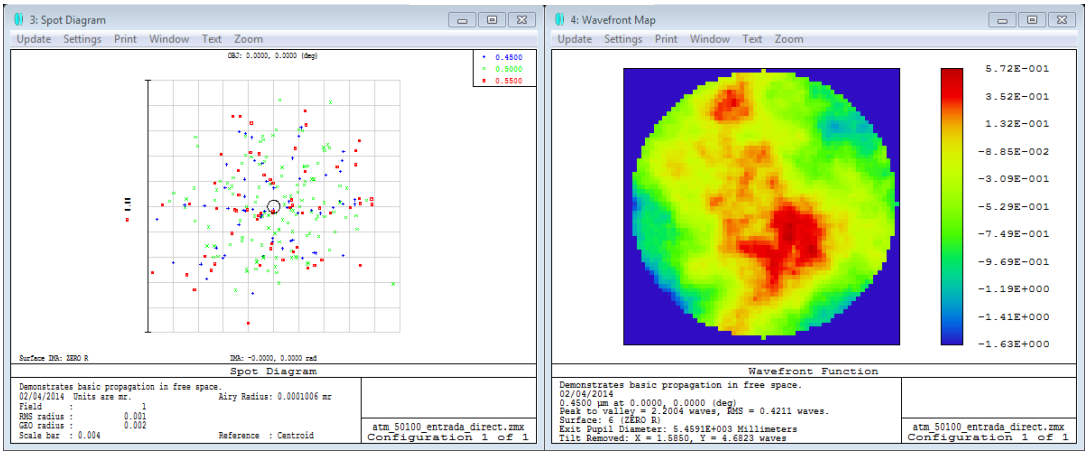

Direct case

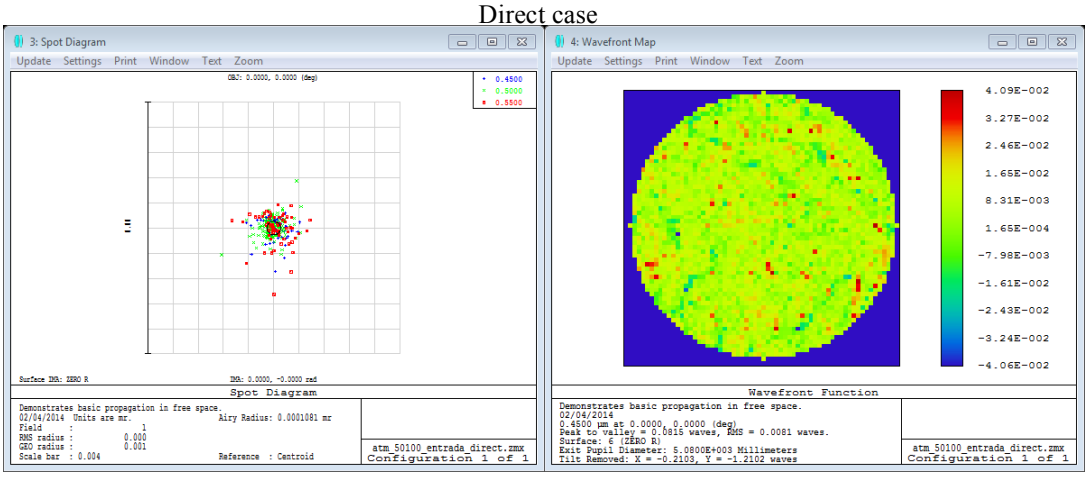

Indirect case

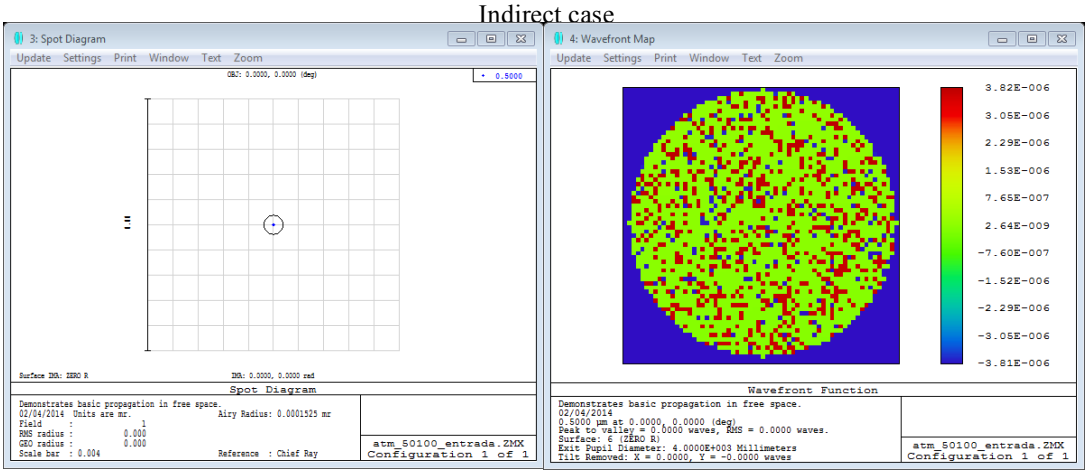

Figure 10. Spot Diagram and residual wavefront map in the image plane. From top to bottom: no correction case, direct case and inverse case.

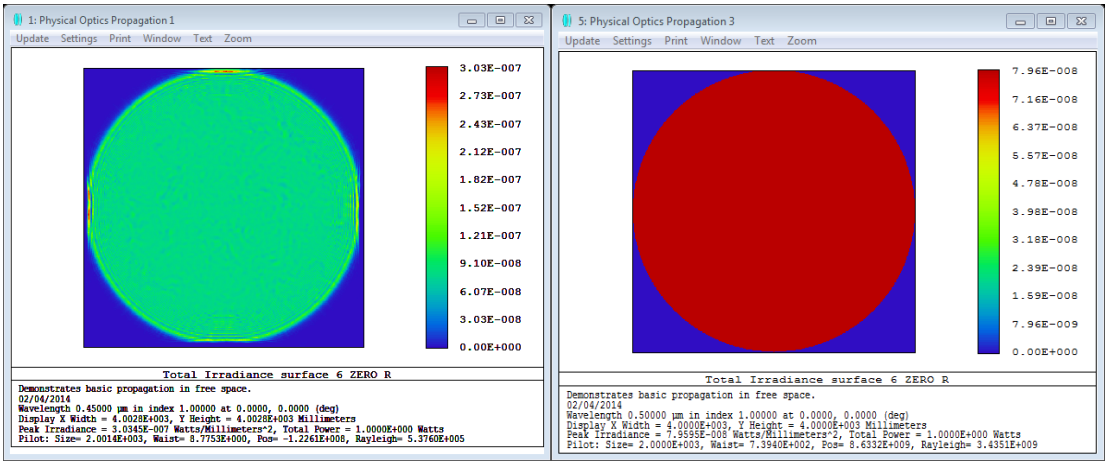

Figure 11 .Irradiance of propagated beam after last surface in direct case (left) and inverse case (right)

2: RMS vs. Field 2

Update Settings Print Window

```
Title: Demonstrates basic propagation in free space.
Date : 05/05/2014


Strehl Ratio is dimensionless.
Reference: Centroid.
Field units are in degrees.
Field is oriented along the +y direction.

       Field     0.4500     0.5000     0.5500
   0.00E+000     0.9980     0.9975     0.9969
   6.67E-008     0.9980     0.9975     0.9969
   1.33E-007     0.9980     0.9975     0.9969
   2.00E-007     0.9980     0.9975     0.9969
   2.67E-007     0.9980     0.9975     0.9969
   3.33E-007     0.9980     0.9975     0.9969
   4.00E-007     0.9980     0.9975     0.9969
   4.67E-007     0.9980     0.9975     0.9969
   5.33E-007     0.9980     0.9975     0.9969
   6.00E-007     0.9980     0.9975     0.9969
   6.67E-007     0.9980     0.9975     0.9969
   7.33E-007     0.9980     0.9975     0.9969
   8.00E-007     0.9980     0.9975     0.9969
   8.67E-007     0.9980     0.9975     0.9969
   9.33E-007     0.9980     0.9975     0.9969
   1.00E-006     0.9980     0.9975     0.9969
```

Table 1. Strehl Ratio values for the direct case correction

1.2 GEOMETRICAL APPROACH

Once we have identified that non-linear effects of wavefront propagation are not negligible the goal is to quantify those effects. Wavefront propagation can be studied using physical optics or geometrical optic theory.

With the aim of verifying the results obtained with ZEMAX, a script in *yorick* based on the geometrical propagation of the wavefront was developed. The paraxial approximation is applied, that means small wavefront errors and small ray angles. The surfaces are assumed infinitely thin.

Each ray has associated coordinates x_0, y_0, incident angles α_{x0}, α_{y0}. The ray propagated along a distance z has the following coordinates when it arrives to surface 1:

$$x_1 = x_0 + \alpha_{x0}\Delta z$$

$$y_1 = y_0 + \alpha_{y0}\Delta z$$

$$\alpha_{x1} = \alpha_{x0}$$

$$\alpha_{y1} = \alpha_{y0}$$

The optical path length (OPL) associated to each ray when it arrives to surface 1 is:

$$OPL_1 = OPL_0 + \Delta z\left[1 + \frac{\alpha_{x0}^2 + \alpha_{y0}^2}{2}\right]$$

The refracting ray after passing surface 1 has the following coordinates:

$$x'_1 = x_1$$

$$y'_1 = y_1$$

$$\alpha'_{x1} = \alpha_{x1} + \frac{\partial OPS_1}{\partial x}$$

$$\alpha'_{y1} = \alpha_{y1} + \frac{\partial OPS_1}{\partial y}$$

The OPL after refracting on surface 1 is:

$$OPL'_1 = OPL_1 + OPS_1$$

where OPS_1 is the phase of surface 1 in the position of the refracting ray.

This formalism allows to calculate the ray tracing trough a set of surfaces and create the phase wavefront map after propagation.

The propagation including the irradiance variations is also simulated. To this aim, the grid is divided onto areas defined by four rays, as shown in Figure 12.

Figure 12. Ray grid structure left: at the entrance, right: after surface distortion

The irradiance per area has to be constant at each surface, that is:

$$I_1 A_1 = I_2 A_2$$

As the position of rays is known at each surface it is possible to calculate the areas and thus generate an irradiance wavefront map.

A set of 1225 rays over a 512 grid of 4m size is simulated. A system formed of two turbulent layers at 1 Km and 15Km with r0 of 8 cm and 10 cm respectively is generated. The cases of direct and inverse correction are studied.

In Figure 13, the phase and irradiance wavefront maps are shown for both cases. As expected with the direct correction the amplitude and phase are not totally cancelled. Nevertheless, in the inverse case the correction should be perfect and small phase residue remains. This is due to the limitations of the geometrical approach. The results are strongly dependent on the configuration parameters, spatial sampling of phase screen, spatial sampling of ray grid. This approach is only valid for the case of soft wavefront errors.

In conclusion, the geometrical approach is not the adequate method to present the wavefront propagation.

The next step of the study is to perform a physical propagation analysis.

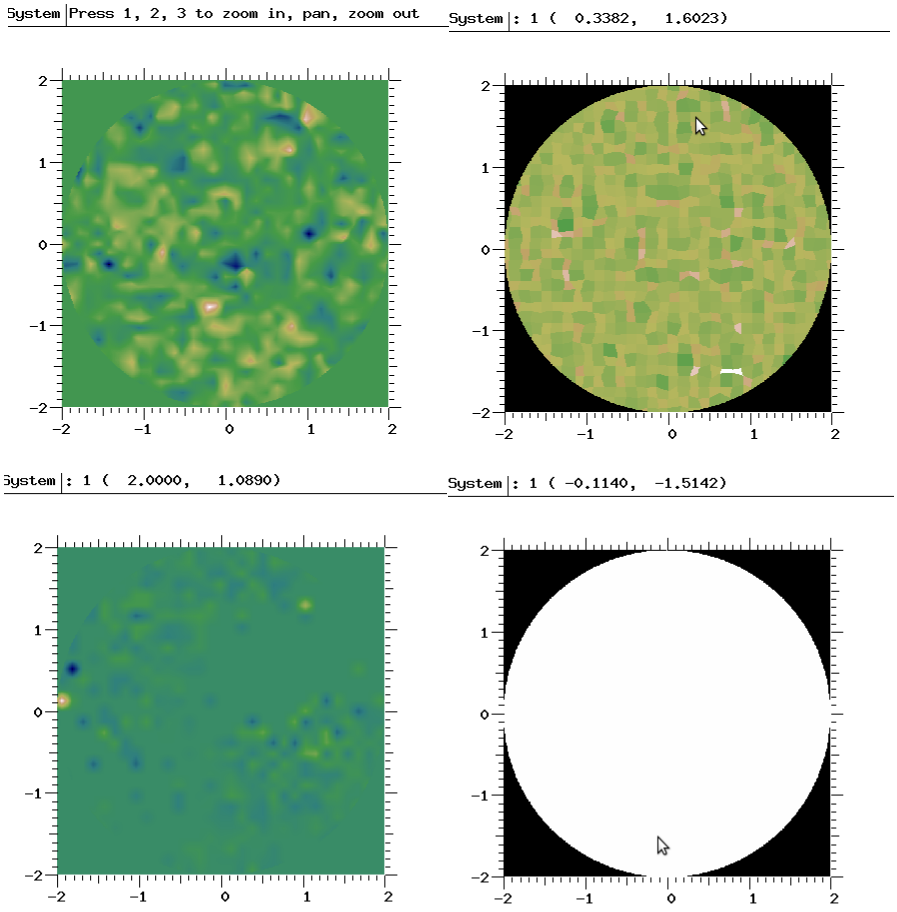

Figure 13. residual phase (left) and irradiance (right) for direct (top) and inverse (bottom) correction

2. MCAO SIMULATIONS

One of the milestones of the SOLARNET MCAO package is to build a simulation environment for Solar MCAO.

The astronomy community has been working on AO simulation codes during decades. Those tools are optimised for night astronomy, however to date none of the codes is suitable for the solar case.

The aim is to complete the existing codes with the special features of the solar case. We have chosen two codes developed in *yorick:*

- YAO: is a Monte-Carlo simulation tool for adaptive with a large number of capabilities and the possibility of implementing custom functions (RD.3). It is an end-to-end simulation code.
- FRiM-3D (the Fractal Iterative Method for Atmospheric Tomography): is a simulation tool for AO based in a geometrical model with a powerful reconstruction algorithm.(RD.4). It has not implemented the close loop capability.

During 2014 a set of simulations have been performed with FRiM-3D as already described in RD.5.

We are currently getting familiar with YAO code with the aim of comparing the results obtained with FRiM-3D. Up to now we have run a MCAO simulation with five natural guide stars and 2 DMs. In Figure 14 the image of 5 Shack-Hartmann WFS, the corrected image in the focal plane, the residual wavefront error and the DM shapes. The Table 2 shows that the correction is uniform in terms of Strehl over the whole field of view.

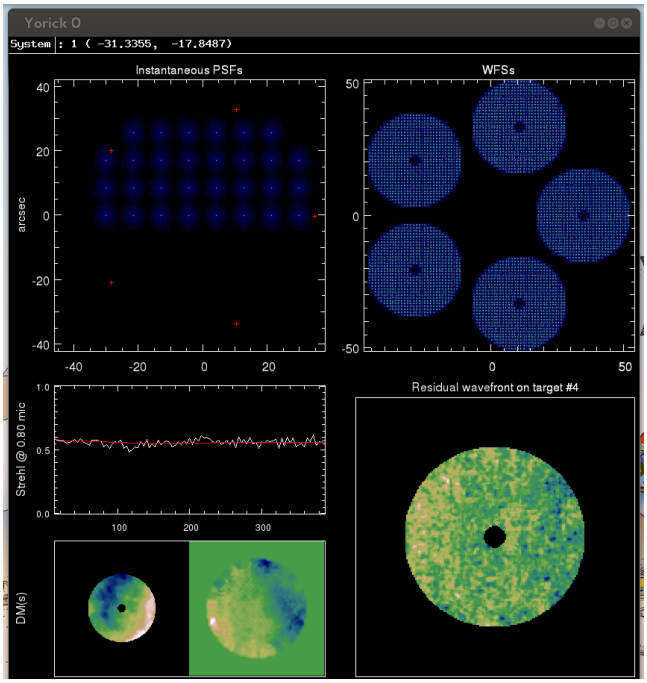

Figure 14. Screenshot of MCAO simulation with YAO.

```
Finished on 15:18:00
8.996366 iterations/second on average
 Pixel size in images (e.g., imav): 10.314 mas

         lambda   XPos   YPos  FWHM[mas]  Strehl  E50d[mas]
Star# 1    0.80  -30.0    0.0       21.6   0.559       54.3
Star# 2    0.80  -21.4    0.0       21.6   0.574       51.7
Star# 3    0.80  -12.9    0.0       21.8   0.573       51.7
Star# 4    0.80   -4.3    0.0       22.0   0.568       51.7
Star# 5    0.80    4.3    0.0       21.8   0.565       51.7
Star# 6    0.80   12.9    0.0       21.6   0.556       54.3
Star# 7    0.80   21.4    0.0       21.6   0.552       54.3
Star# 8    0.80   30.0    0.0       21.8   0.557       49.1
Star# 9    0.80  -30.0    8.6       21.6   0.571       49.1
Star#10    0.80  -21.4    8.6       22.0   0.579       49.1
Star#11    0.80  -12.9    8.6       22.0   0.571       51.7
Star#12    0.80   -4.3    8.6       22.2   0.566       51.7
Star#13    0.80    4.3    8.6       22.2   0.562       51.7
Star#14    0.80   12.9    8.6       22.0   0.557       51.7
Star#15    0.80   21.4    8.6       21.6   0.550       54.3
Star#16    0.80   30.0    8.6       21.8   0.546       51.7
Star#17    0.80  -30.0   17.1       21.8   0.580       46.5
Star#18    0.80  -21.4   17.1       22.0   0.582       46.5
Star#19    0.80  -12.9   17.1       22.0   0.568       51.7
Star#20    0.80   -4.3   17.1       22.0   0.564       51.7
Star#21    0.80    4.3   17.1       22.0   0.564       51.7
Star#22    0.80   12.9   17.1       22.0   0.560       51.7
Star#23    0.80   21.4   17.1       21.8   0.549       51.7
Star#24    0.80   30.0   17.1       21.8   0.529       56.8
Star#25    0.80  -21.4   25.7       21.8   0.564       51.7
Star#26    0.80  -12.9   25.7       22.0   0.557       54.3
Star#27    0.80   -4.3   25.7       21.8   0.557       54.3
Star#28    0.80    4.3   25.7       21.8   0.567       49.1
Star#29    0.80   12.9   25.7       21.6   0.567       46.5
Star#30    0.80   21.4   25.7       21.8   0.546       51.7
Field Avg  0.80                     21.8   0.562       51.5
Field rms  0.80                      0.2   0.011        2.4
```

Table 2. Strehl ratio over a field of view of 1'.

One of the key points of the AO simulation is the reconstruction method. The reconstruction can be seen as two steps. One is the tomographic reconstruction of the turbulent volume. It depends on the guide star configuration and atmospheric conditions. Second, the projection of the tomographic measurements onto the DMs. It depends on the number and positions of the DMs. Up to now the DMs have been placed at the heights where turbulence has been measured. The performance could improve projecting a turbulent volume into DMs as proposed by Neichel et al. (RD.4). We are in the process of implementing the projector in both codes.

Once the codes will be tested, the goal is to use a combined tool, using YAO as a physical simulator with FRiM-3D reconstruction algorithm. For this purpose special operators, such the extended WFS need to be implemented in YAO.

3. CONCLUSIONS

ZEMAX has been used for the study of the wavefront propagation. Two approaches have been studied. In the paraxial approach although the ray tracing is correct the wavefront analysis is incorrect. Therefore a second approach using geometric propagation in the entrance space is studied. As expected, the correction in the inverse case is perfect and the residual wavefront error is zero, while in the direct case the correction, although still very good, is not perfect. The correction in the direct case could be perfect if reconstruction algorithms were implemented in the simulations.

Our study based on the ZEMAX tool does not allow verifying the effect of scintillation on wavefront propagation. A script in *yorick* has been developed using a geometrical approach but including the irradiance propagation but the results are strongly dependent on the sampling parameters. Therefore, wavefront propagation using physical models will be implemented in future simulations to quantify the effects of sequence of phase correction.

We are currently adapting two existing codes for AO: YAO and FRiM for the Solar case.

ANNEXES

A. LIST OF REFERENCE DOCUMENTS

RD.1	YOUNG, “Seeing: its cause and cure”,ApJ,189,1974
RD.2	Flicker, “Sequence of phase correction in multiconjugate adaptive optics”, Optics Letters,26,2001.
RD.3	FOUCHÉ et al, “Correction of scintillation effects by multiconjugate adaptive optics”, Proc.SPIE 2001
RD.4	Neichel et al, “Tomographic reconstruction for Wide Field Adaptive Optics systems: Fourier analysis and fundamentals limitations”,JOSA,26,2008
RD.5	DO/TN-SNT/019v.1, WP 70.1 MCAO simulations 1/2(D70.1)